Final Draft
of the original manuscript:

Chaudhary, A.-L.; Sheppard, D.A.; Paskevicius, M.; Pistidda, C.; Dornheim, M.; Buckley, C.E.:

Reaction kinetic behaviour with relation to crystallite/grain size dependency in the Mg–Si–H system

Reaction kinetic behaviour with relation to crystallite/grain size dependency in the Mg-Si-H system

*Anna-Lisa Chaudhary[*1,2], Drew A. Sheppard[1], Mark Paskevicius[1], Claudio Pistidda[2], Martin Dornheim[2], Craig E. Buckley[1]*

[1] Department of Physics, Astronomy and Medical Radiation Sciences, Curtin University, GPO Box U1987, Perth 6845, WA, Australia ,

[2] Department of Nanotechnology, Institute of Materials Research, Helmholtz-Zentrum Geesthacht, Max-Planck-Strasse 1, D-21502 Geesthacht, Germany

Abstract

An empirical understanding of the relationship between crystallite size and reaction kinetics for the dehydrogenation of MgH_2 in the presence of Si was determined. MgH_2 was combined with Si under different processing conditions to obtain varying crystallite sizes of both reactants. Differential scanning calorimetry and isothermal desorption were undertaken to obtain reaction kinetic information and therefore determine activation energies as well as the rate limiting step for each of the different crystallite sizes. It was found that there is a strong correlation between crystallite size and activation energy for the growth of the Mg_2Si phase, however, any correlation between the nucleation (of Mg_2Si) activation energy was less evident. Direct measurements of kinetic behaviour from a manometric Sieverts apparatus showed that initial reaction kinetics are fastest when MgH_2 was mixed with Si nanoparticles, however, this reaction was not able to fully desorb. Data from the Sieverts apparatus was then used with well-known theoretical models to determine the rate limiting step of the reaction. For most of the samples the three dimensional Carter-Valensi (or contracting volume) diffusion model could be used to describe the rate limiting step of the reactions. A proposed mechanism has been given and discussed for the formation of Mg_2Si during the decomposition reaction.

Keywords

Activation energy, Kissinger method, magnesium silicon hydrogen system, reaction kinetic modelling, light weight metal hydrides, hydrogen storage

Introduction

Hydrogen sorption kinetics of metal hydrides describes the rate at which hydrogen is absorbed into or released from a metal matrix at a certain temperature, hydrogen pressure and applied voltage. Owing to a gravimetric hydrogen storage capacity of 7.7 wt.%, high energy density (9 MJ/kg Mg)[1] and relatively low cost[2], in the last decades, many authors have investigated the hydrogen sorption properties of MgH_2. A major drawback of this material was its rather sluggish sorption kinetics which hindered practical use as a hydrogen storage material. Aiming to understand the reasons which stood behind the observed kinetic barriers, [3-6] many authors have focused their attention on studying the hydrogen sorption kinetics of MgH_2 in terms of the rate limiting step. According to Minz et. al., hydrogen absorption, of Mg can be described as a three dimensional diffusion reaction following a nucleation and growth mechanism [7]. It has been suggested that this nucleation step could be gas pressure dependent and therefore could be the rate limiting step for initial hydrogenation [4], however, other studies have shown that diffusion of hydrogen through the MgH_2 phase controls hydrogenation [8, 9]. Growth of MgH_2 occurs at the interface between hydrogen gas and magnesium and grows inward from the particle surface [4] and proceeds faster along lattice defects such as dislocations and vacancies [10]. Studies have also shown that this behaviour can change with the addition of a catalyst such as Nb_2O_5 [11-13] where the reaction was shown to be diffusion controlled along the boundary of the magnesium/hydride phases.

**Eqn. 1** $\quad\quad\quad Mg(s) + H_2(g) \leftrightarrow MgH_2(s)$
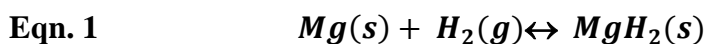
In the literature three main barriers to fast absorption kinetics are reported for the Mg-H system. The first point to consider is the strong affinity of magnesium to oxygen and the resulting surface oxide/hydroxide layer [14-17] that acts as a physical barrier for the chemisorption of hydrogen. Secondly, hydrogen dissociation on a clean Mg surface has a high activation energy [18]. Thirdly, for particle sizes larger than 30 – 50 μm, the hydride layer impedes hydrogen diffusion and further hydrogenation does not proceed to completion in a suitable timeframe [3]. Strategies to improve the hydrogen absorption into Mg have been developed to increase the kinetic rate. These strategies include crystallite/grain size reduction [19-23] and catalyst addition [24-26]. However, recent studies suggest that "catalyst" addition may have multiple functions such as acting as a grain size stabiliser, as nucleation sites for a reaction to proceed [27], as a refining agent that reduces the grain/crystallite size during ball milling [28], or to improve pathways for fast hydrogen diffusion [29]. Since most of the literature agrees that the

rate determining step is the diffusion of hydrogen through the MgH_2 phase [8, 20, 30], this suggests that grain or crystallite size reduction due to ball milling may have a significant influence on reaction kinetics.

With respect to hydrogen desorption, or dehydrogenation, a one-step, direct path has been identified, where two hydrogen atoms, bound to different Mg atoms, simultaneously desorb [31]. For the dehydrogenation reaction to occur, magnesium has to be nucleated and continue to grow whilst the hydrogen atoms diffuse to the surface and recombine to form H_2 molecules [24]. Each of these steps could be linked to the thermal transitions found in the DSC data but there has been little evidence in the literature to support this theory. Despite this, there is a strong consensus with regard to desorption reaction mechanisms, as studies have agreed that nucleation is followed by interface controlled growth [3, 8, 20, 23].

When analysing the Mg-Si-H system (Eqn. 2), H is more likely to bond with Mg not Si, because SiH_4 formation is highly endothermic [32] and is therefore not thermodynamically favourable. Thermodynamic calculations have shown that the addition of silicon to magnesium hydride significantly reduces the thermodynamic stability of the system [32-34] to an equilibrium of 1 bar of hydrogen pressure at room temperature. Experimentally, these conditions have never been met, hence the conclusion that reaction kinetics play a dominant role in the desorption reaction. Nano-scale particle sizes and crystallite sizes can overcome slow diffusion rates by reducing overall diffusion distances [35, 36] since a reduction in grain size also enhances the net reaction rate by increasing surface area and interfacial contact between different phases [37]. Thus, the crystallite or grain size may improve the rate of diffusion of Mg through the Si atoms to obtain Mg_2Si [38]. Our hypothesis is that if the crystallite sizes of the reactants are small enough, the kinetic enhancement would allow for hydrogen evolution to proceed at much lower temperatures and may also allow for hydrogen absorption to occur under modest conditions [35, 39]. Presented here is a kinetic hydrogen desorption study involving MgH_2 with Si prepared using different methods to obtain different crystallite sizes (or grain size in the case of amorphous Si nanoparticles).

Eqn. 2 $\qquad 2MgH_2(s) + Si(s) \rightarrow Mg_2Si(s) + 2H_2(g)$
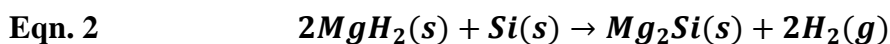
Materials and Methods

All samples were handled in a controlled Ar atmosphere glove box (Unilab Glovebox, mBraun, Germany) with an automatic gas purifier unit that maintained low levels of O_2 (< 1 ppm) and

(H₂O < 1 ppm). Six samples of MgH_2 (Sigma Aldrich, H_2 storage grade, 95%) were mixed with Si powder (Sigma Aldrich, − 325 mesh, 99%). Samples (A) – (E) (Table 1) were prepared using the as supplied Si, but the final sample, (F), used Si nanoparticles (NP, ~13 nm) that were synthesised in a method described in [36]. Six mixtures of 2:1 molar MgH_2:Si were prepared using different methods to obtain a range of crystallite and grain sizes. Sample (A) was the as supplied sample, representing bulk unmilled materials, and was prepared by hand mixing $2MgH_2$ + Si in a vial for 5 min. Sample (B) was also placed in a vial with tetrahydrofuran (THF) to undergo mixing *via* ultrasonication. The THF was then evaporated under vacuum. Sample (C) was ball milled in a Glen Mills Turbula T2C Shaker-Mixer at 160 rpm for 2 h with a ball to powder ratio (BTP) of 10:1. Both the canister and balls were made from stainless steel 316. Sample (D) was cryomilled for 2 h at 77 K in a Spex 6850 freezer mill. Sample (E) was also ball milled in the Glen Mills Turbula (160 rpm) for a longer time, 24 h with a high BTP ratio of 30:1. The NP Si containing sample (F) was cryomilled for 30 min with MgH_2. This MgH_2 was ball milled prior to cryomilling with a BTP ratio of 90:1 for 18 h to obtain small particles with limited contamination from the stainless steel milling media.

X-Ray diffraction (XRD) measurements were conducted using a Bruker D8 Advance X-ray diffractometer (Germany) with Bragg-Brentano geometry and a copper X-ray tube (λ = 1.5418 Å). A 2θ range of 10° – 100° with a step size of 0.02° and 0.7 s of count time per step was used. All materials were analysed in a Bruker supplied airtight specimen holder ring with dome type, X-ray transparent polymethylmethacrylate (PMMA) cap and the Si NP containing sample was characterised using Al foil as a protective layer as outline in [36]. Crystallite size values were taken from the LVol-IB (volume weighted mean column height) that incorporates Lorentzian and Gaussian convolutions varying in 2θ as a function of $\cos(\theta)^{-1}$ and $\tan(\theta)$ respectively (*Diffracplus TOPAS* Version 4.2). This method provides a volume weighted average crystallite size. Uncertainties were reported from *TOPAS* (bootstrap method of error determination).

A Zeiss Neon 40EsB (Germany) scanning electron microscope (SEM) was used for high resolution SEM. Samples were prepared on an aluminium SEM stub without carbon tape. The SEM stubs were then coated with a 2 – 4 nm coating of high atomic elements, either gold or platinum to produce a conductive layer and reduce charging of the sample during its interaction with the electrons in the SEM. All samples were exposed to air for a short period of time (minutes) when in and out of the coating instrument as well as loading into the SEM chamber.

Thermal analysis was undertaken using a DSC 6000 (Perkin Elmer, Waltham, Massachusetts, USA) with a cryofill liquid nitrogen cooling system. 10 mg ($\pm$ 10%) samples were weighed into aluminium pans and hermetically sealed in an Ar atmosphere glovebox. The sample filled pan was placed in a furnace chamber with a reference pan, an empty hermetically sealed aluminium pan. 10 mg ($\pm$ 1 mg) of the Mg-H-Si mixtures were placed into the pans to ensure any changes in pressure inside the pan were comparable between samples. Nitrogen was used as the purge gas at a rate of 20 mL min^{-1} in the furnace chamber to reduce any influence of water or air on the measurements during the experiment, even though the crucibles were sealed. The chamber was heated at a constant rate according to the programmed heating ramp (2, 5, 7, or 10 °C min^{-1}) from 25 °C to 450 °C. The maximum achievable pressure inside the pan was calculated to be approximately 15 bar at 450 °C, far below the thermodynamic equilibrium for this system [34]. Data were recorded and analysed using Pyris Thermal Analysis software (Perkin Elmer, Version 10.1.0412, 2009).

Isothermal dehydrogenation kinetic data were obtained using a manometric Sieverts apparatus. The sample was held isothermally in a furnace at 300°C and hydrogen release was measured over time (24 h). Rosemount pressure transducers model 3051S, precision 0.01%, accuracy 0.02%, were used to monitor pressure. The room temperature was measured using either a K-type thermocouple or a RTD 4-wire platinum thermistor whilst thermocouples used to measure the temperature of the sample were either K-type or N-type.

Results and Discussion

Crystallite and Particle Size Determination

XRD Rietveld analysis (Figure 1) was used to calculate the crystallite size (Table 1) for each of the six MgH$_2$/Si mixtures. The samples listed in Table 1 have been arranged in descending order of crystallite size for MgH$_2$ and Si from (A) to (F). Since the Si NPs were not crystalline, the diameter measured from SAXS [36], 13 nm, was used. The XRD patterns (Figure 1) show that the crystallite size decreases from more intense milling, with peak broadening for both MgH$_2$ and Si apparent, and that the final plot, (F), does not show Si due to its amorphous nature [36].

One point to note is the presence of the γ-phase of MgH$_2$ in the samples that have undergone a milling process. This polymorph is typically seen in samples that have been subjected to the

GPa range of pressures and temperatures up to 900°C although evidence suggests that room temperature experiments can also result in the formation of this phase [40], especially after high energy milling [20, 41]. There are two sources of obvious contamination. Firstly, the MgH_2 from Sigma Aldrich is only 95% pure, the remainder being Mg and likely a small quantity of MgO. Secondly, the materials that underwent either ball milling or cryomilling had a trace amount of SS316 present due to their interaction with the milling media.
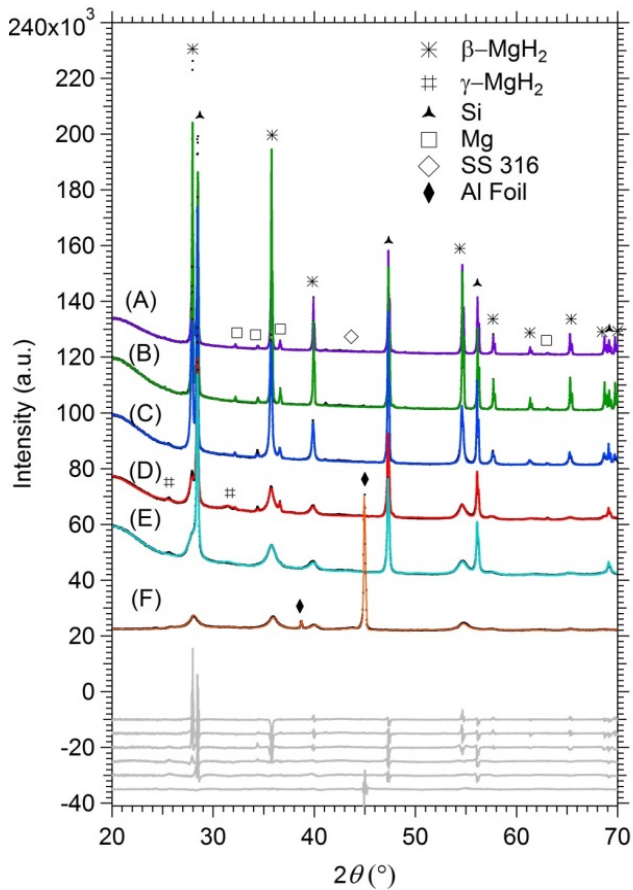
Figure 1: XRD patterns of $2MgH_2$ + Si (A) mixed in a vial by hand for 5 min (purple) (B) ultrasonicated in THF (green) (C) ball-milled BTP 10:1 2 h (blue)(D) cryomilled for 2 h (red) (E) ball-milled BTP 90:1 24 h (cyan) (F) ball-milled MgH_2 for 18 h with synthesised Si nanoparticles, 13 nm (orange). The coloured plots of the calculated Rietveld refinement overlay the raw XRD data. The grey plots below represent the difference between the Rietveld and raw data from (A) at the top to (F) at the bottom.

Table 1: Rietveld analysis of the $2MgH_2$ + Si mixtures.

$2MgH_2$ + Si	Phase	Crystallite Size (nm)
(A) Hand Mixed 5 min	MgH_2	207 ± 3
R_{wp} = 5%	Mg	174 ± 33
	Si	173 ± 3
(B) Ultrasonicated	MgH_2	201 ± 3
R_{wp} = 5.5%	Mg	194 ± 36
	Si	169 ± 3

(C) Ball-milled 2 h	β-MgH₂	40 ± 1
R_{wp} = 6.2%	γ-MgH₂	14 ± 7
	Mg	70 ± 11
	Si	134 ± 2
(D) Cryomilled 2 h	β-MgH₂	10 ± 1
R_{wp} = 4.1%	γ-MgH₂	5 ± 1
	Mg	72 ± 10
	Si	63 ± 1
(E) Ball-milled 30:1 24 h	β-MgH₂	6 ± 1
R_{wp} = 3.8%	γ-MgH₂	3 ± 1
	Mg	-
	Si	46 ± 1
(F) Ball-milled MgH₂ 18 h + NP Si	β-MgH₂	6 ± 1
R_{wp} = 4.5%	γ-MgH₂	2 ± 1
	Si	13 nm amorphous Si

SEM shows the morphology of the ultrasonicated, cryomilled and ball milled (for 2 h) samples (Figure 2). Figure 2a, c and e used secondary electrons to give clear images of the surface morphology, particularly grain size and shape. Figure 2b, d and f are images using backscattered electrons where darker shades typically indicate lighter elements. In this case, MgH₂ has a lower molecular weight compared to Si, therefore, MgH₂ is slightly darker in colour than the Si particles [33]. Ultrasonicated particles are the largest with the majority being $\geq$ 10 μm with a small volume of finer particles. Ball milling at a BTP ratio of 10:1 for 2 h gave significantly smaller particles. Cryomilling for 2 h reduced the particle size even further to $\leq$ 10 μm although some bigger particles are also present, possibly in the form of aggregates.
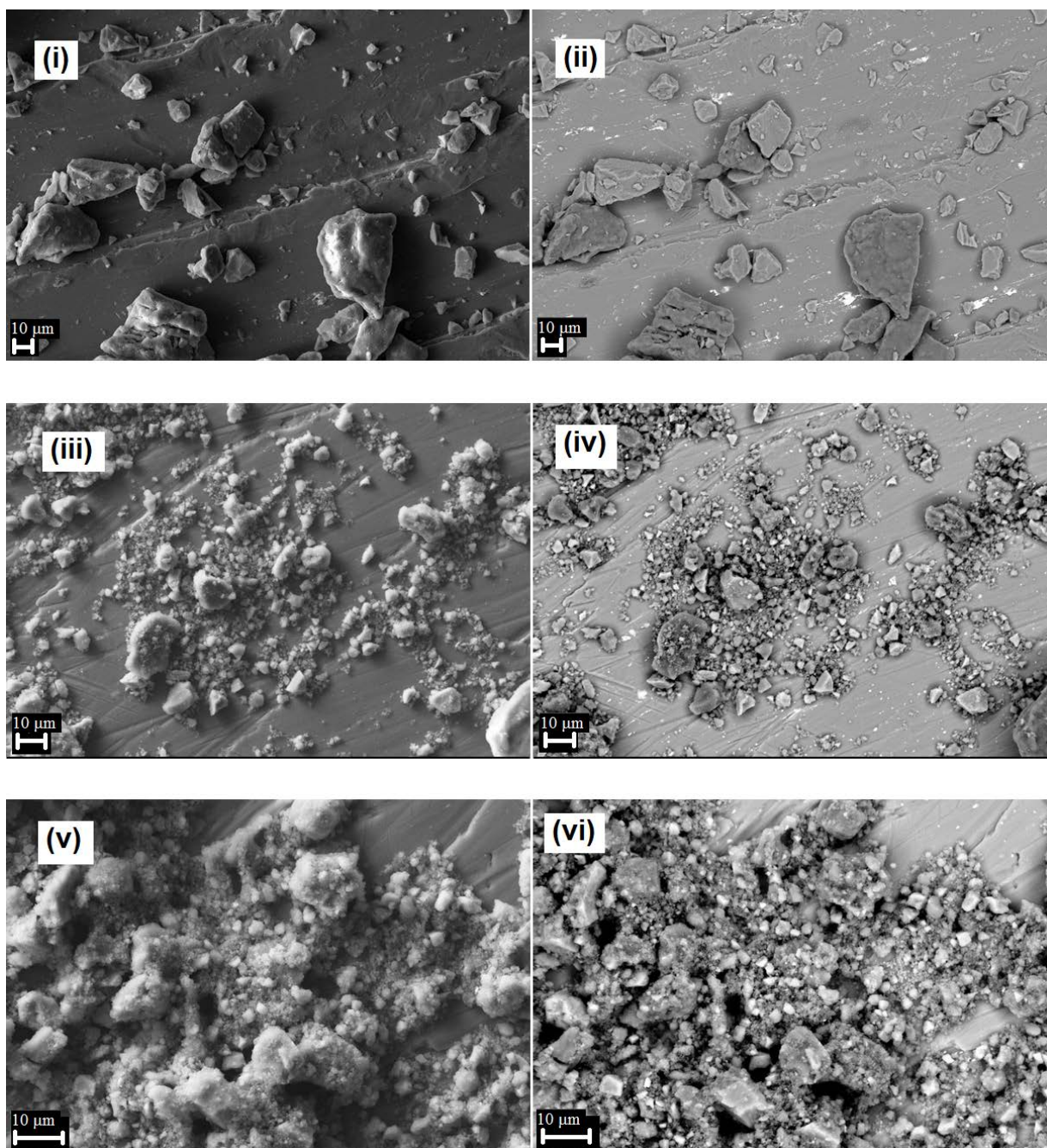
Figure 2: SEM micrographs of 2MgH$_2$ + Si (i) sample (B) ultrasonicated in THF, SE image, (ii) sample (B) ultrasonicated in THF, BSE image, (iii) sample (C) ball-milled BTP 10:1 2 h, SE image (iv) sample (C) ball-milled BTP 10:1 2 h, BSE image, (v) sample (D) cryomilled for 2 h, SE image, (vi) sample (D) cryomilled for 2 h, BSE image.

There are several important observations that can be made when comparing the SEM BSE images shown in Figure 2b, d and f. The materials prepared using ultrasonication show two distinct size distributions, each from the MgH$_2$ and Si phases. As the MgH$_2$ particle size undergoes reduction *via* ball milling or cryomilling the distinction between the two phases is less pronounced. For all of the images in general, Si particles (brighter shades in BSE images)

are smaller and are more evenly distributed amongst the MgH_2 particles in the ball milled and cryomilled samples. The different samples show differing degrees of homogeneity depending on the mixing method. The degree of homogeneity of the reactants is a key feature of the sample as the kinetic reaction mechanism is highly dependent on how well the phases are mixed [42].

Desorption Reaction Kinetics

The Kissinger method [43, 44] can be used to calculate the activation energy of the rate controlling process based on data obtained from thermal analysis. The Kissinger method takes the heating rate, β, and the maximum reaction rate peak temperature, T_{max}, to determine the reaction rate barrier, otherwise known as the activation energy, E_a (Eqn. 3). R is the universal gas constant. DSC data are given in Figure 3 and show that each material underwent one or more thermal transitions dominated by a single thermal event. All transitions are endothermic and the main thermal event can be attributed to the decomposition of MgH_2 in the presence of Si. Below 100°C there are no significant events, indicated by the flat baseline. For the purposes of this study, two temperatures are identified as two mechanisms from the DSC data, the onset temperature (T_o) and the maximum temperature (T_{max}). T_o was associated with the nucleation mechanism ($T = T_o$, Eqn. 3), to determine the activation energy associated with nucleation, E_n. T_{max} was used to determine E_a which represents the activation energy for the growth of the new phases from the reaction ($T = T_{max}$, Eqn. 3).

Eqn. 3:
$$\frac{dln\left(\frac{\beta}{T^2}\right)}{d\left(\frac{1}{T}\right)} = -\frac{E_A}{R}$$

DSC data from the ultrasonicated sample, Figure 3.1, gives a single transition at temperatures > 400°C, the highest of all the samples. The large grain and crystallite sizes can account for this transition occurring at these high temperatures. Due to the limitations of the DSC (a maximum operating temperature of 450°C), it is possible that larger grains within this sample could desorb at even higher temperatures and hence not be detected here. Similarly, the temperature limitation of the instrument did not show accurate thermal transitions for the hand milled sample, hence the activation energies could not be measured.

Figure 3.2 displays more than one thermal transition for the 2 h ball milled sample with a BTP ratio of 10:1. The various heating rate curves for this material appear to undergo a three phase

decomposition mechanism similar to that of pure MgH_2 [45] with a double peak between 350°C and 450°C, depending on the heating rate. These peaks, in part, are due to the broad range of MgH_2 particle sizes within the sample (Figure 3b), where the smaller particles desorb at a lower temperature and the larger particles desorb at a higher temperature.

The remaining DSC curves, cryomilled (Figure 3.3), 24 h ball milled (Figure 3.4) and NP Si with 18 h ball milled MgH_2 (Figure 3.5), show multiple thermal events. Some of this behaviour can be related to the heterogeneous particles sizes of MgH_2 in the samples, however, it could also be due to the different crystalline phases present, as detected by the XRD, γ-MgH_2 and β-MgH_2. The cryomilled sample (Figure 3.3) as well as the sample containing Si NPs (Figure 3.5) show a small thermal event at 270°C and 210°C respectively, almost masked by the onset rise in temperature of the desorption reaction. A previous study showed that γ-MgH_2 completely desorbs at lower temperatures than β- MgH_2 [46]. Partial decomposition of β-MgH_2 does occur at this lower temperature, however, this structure is not completely desorbed until higher temperatures are reached [46] as DSC events are a function of both kinetics and thermodynamics. The 24 h ball milled sample (Figure 3.4) has a less obvious transition occurring at 200°C and 250°C for the 5°C min^{-1} and 10°C min^{-1} heating rates respectively. This is due to the lower concentration of γ-MgH_2 present in these samples (Table 1).
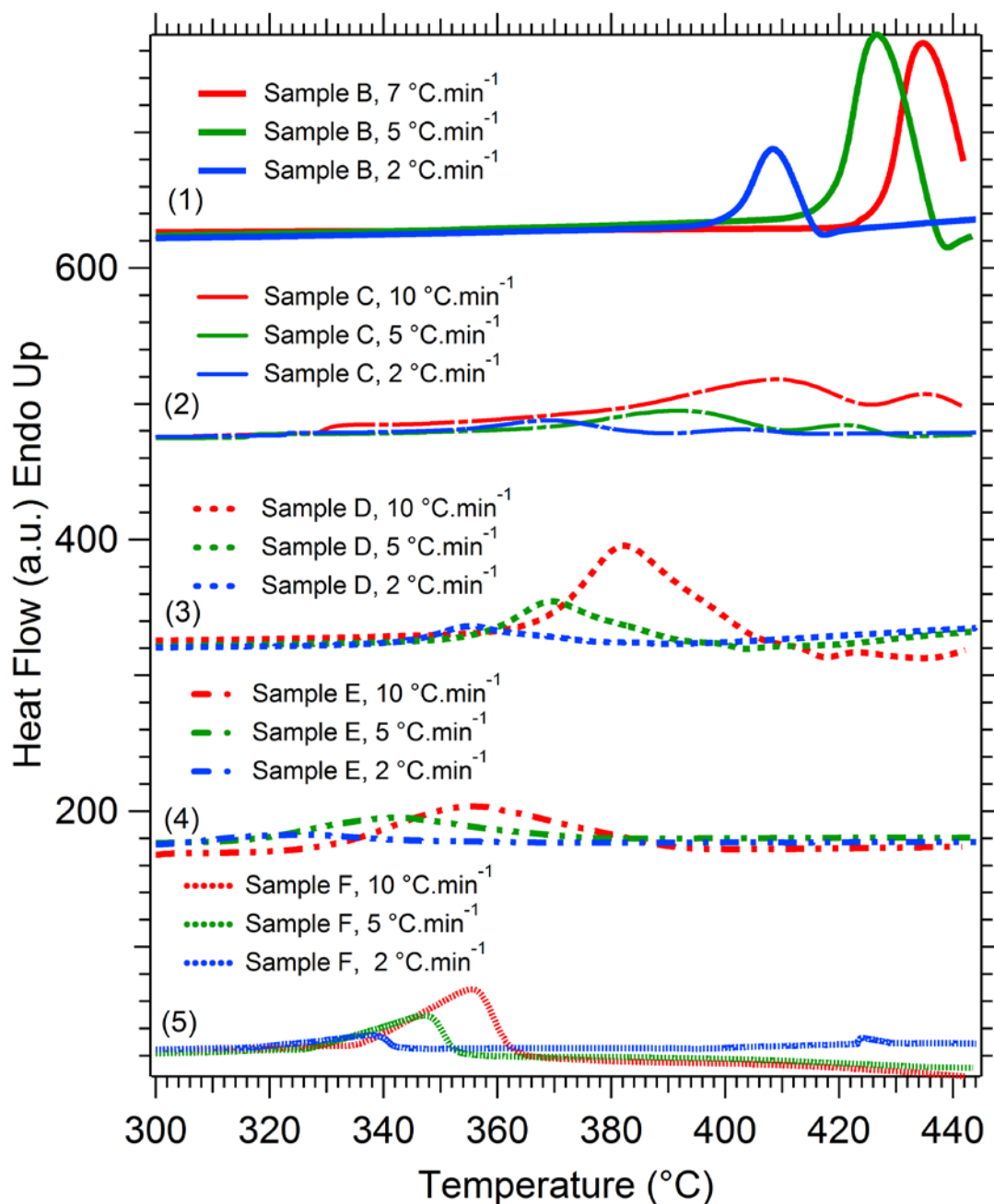
Figure 3: DSC data for MgH₂ + Si mixtures. (1) sample (B) ultrasonicated, (2) sample (C) ball milled 2h, (3) sample (D) cryomilled 2 h, (4) sample (E) ball milled 24 h, (6) sample (F) ball milled 18 h MgH₂ + NP Si.

The calculated activation energies for nucleation and growth are shown in relation to crystallite size in Figure 4. There is no apparent trend that correlates the nucleation activation energy values to crystallite size (or particle size for the nanoparticle Si). The highest nucleation activation energy (E_n) value was not the bulk sized ultrasonicated particles; rather the 2 h ball milled sample gave a value of 355.6 kJ mol⁻¹. However, the lowest value for E_n was 133.5 kJ

mol^{-1} for the 24 h ball milled sample. The lack of an obvious trend suggests that Mg_2Si nucleation is not correlated to crystallite/grain sizes (Figure 4a).

Growth activation energy (E_a) values, on the other hand, give an overwhelming correlation between MgH_2 crystallite size (Figure 4b) with the exception of the Si NP sample. The trend shows that the larger the crystallite, the higher the activation energy thus showing a morphological dependency on activation energies for this system. Figure 4 shows a linear relationship between E_a and crystallite size with an R^2 value of 0.96 if the Si NP sample is excluded. Although the relationship can be fit to a straight line, more data is required for a larger range of crystallite sizes to confirm this relationship.
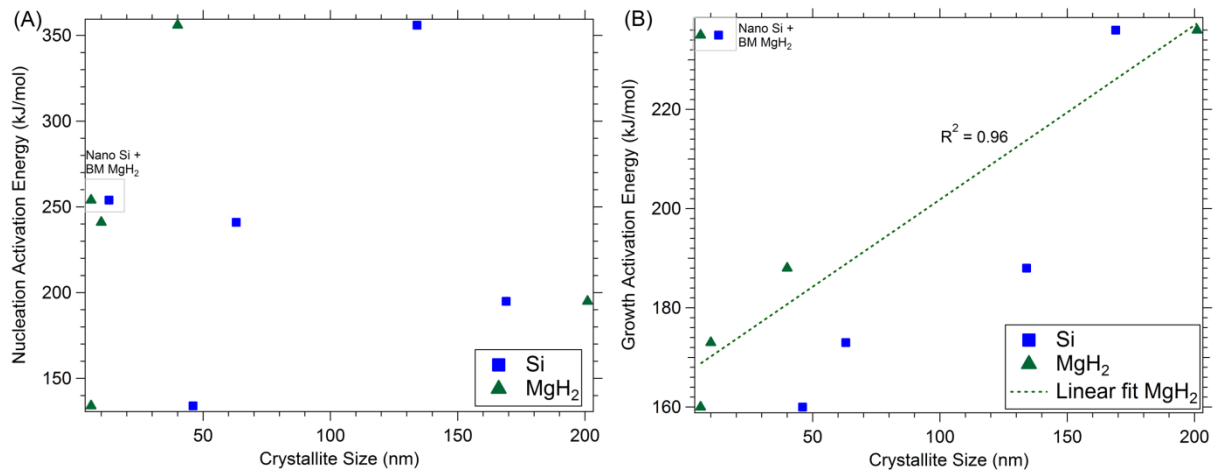
Figure 4: Relationship between Si and MgH$_2$ crystallite sizes and (A) nucleation activation energies, E_n and (B) growth activation energies E_a.

In order to obtain the reaction rate constant, k, the experimental DSC data can be expressed as a function of the transformed fraction, α, from established reaction kinetic models. Solid state kinetic models are a mathematical description of what occurs experimentally and can describe a particular reaction type [47]; in this case, the rate limiting step. The rate limiting step can be determined from the best fit between the experimental data and the proposed models. This method of analysis is detailed in several reaction kinetic publications [11, 48] and the mathematical models are given in Table 2. There are three single particle models that can describe kinetic reaction behaviour: surface reaction [49], Johnson-Mehl-Avrami (JMA) [3-5] and Carter-Valensi/Contracting Volume (CV) [8, 50] models. The surface controlled mechanism is the simplest model that shows that the reaction rate is directly proportional to the

concentration of the remaining reactants [51]. The JMA model applies to nucleation and growth mechanisms occurring randomly at the surface as well as in the bulk phase. The assumption for the JMA model is that hydrogen diffusion is relatively fast and that the rate limiting step is the constant velocity of the intermetallic/hydride interface either two dimensional (2D) or three dimensional (3D). The CV model is different in that it provides for a mechanism that begins with nucleation at the surface of the particle or grain and growth continues from the surface or grain boundary into the bulk. The CV model assumes that nucleation of Mg_2Si on the particle surface is fast and the rate limiting step is either 2D or 3D interfacial growth. This model can also be expressed in terms of 3D diffusional growth.

Table 2: Reaction kinetic model equations where α is the transformed fraction, k is the reaction rate constant, and t, time.

| Model Equation	Description
$\alpha = kt$	Surface controlled mechanism [49]
$[-\ln(1-\alpha)]^{1/2} = kt$	JMA [52-54] 2D interfacial growth
$[-\ln(1-\alpha)]^{1/3} = kt$	JMA [52-54] 3D interfacial growth
$1-[1-\alpha]^{1/2} = kt$	CV [55, 56] 2D interfacial growth
$1-[1-\alpha]^{1/3} = kt$	CV [55, 56] 3D interfacial growth
$1-\left(\dfrac{2\alpha}{3}\right)-(1-\alpha)^{2/3} = kt$	CV [55, 56] 3D diffusional growth

The kinetic decomposition data for each of the six samples are given in Figure 5a. An immediate observation is that the reaction proceeds at a faster rate for smaller crystallite sizes. Again, the only exception being the Si NP sample with ball milled MgH_2, containing amorphous Si. Another interesting point to note is that the 24 h ball milled sample is the only sample that approaches complete desorption in the 24 h time period at 300 °C. The amount of H_2 desorbed from each sample is given in Table 5. As expected, the bulk samples (hand mixed and ultrasonicated) are the slowest due to their larger particle size (Figure 3), and hence MgH_2/Si phase segregation, meaning they release the least amount of hydrogen. Milled materials contain a lot of grain boundaries that act as fast diffusion paths for hydrogen atoms [57] hence the faster reaction rates.

An enhanced view of the reaction data showing the first hour is given in Figure 5b. This plot shows that the 24 h ball milled sample starts at an extremely slow rate similar to that of the 2 h ball milled sample. There is a rapid change in the reaction rate 45 min after the decomposition reaction is initiated. This implies that there is a kinetic barrier present for this sample, possibly due to the presence of an oxidation layer on the MgH_2. All other samples have a constant hydrogen evolution rate from the beginning. Si NP + ball milled MgH_2 has the fastest rate followed by the 2 h cryomilled and 2 h ball milled samples. In order to compare each of the samples with the kinetic models given in Table 5, the data was normalised against the transformed fraction, α, Figure 5c. The hydrogen concentration (wt.%) from the desorption reaction was normalised by dividing by the maximum possible hydrogen release, that is, 5 wt. % to obtain α over 24 h.
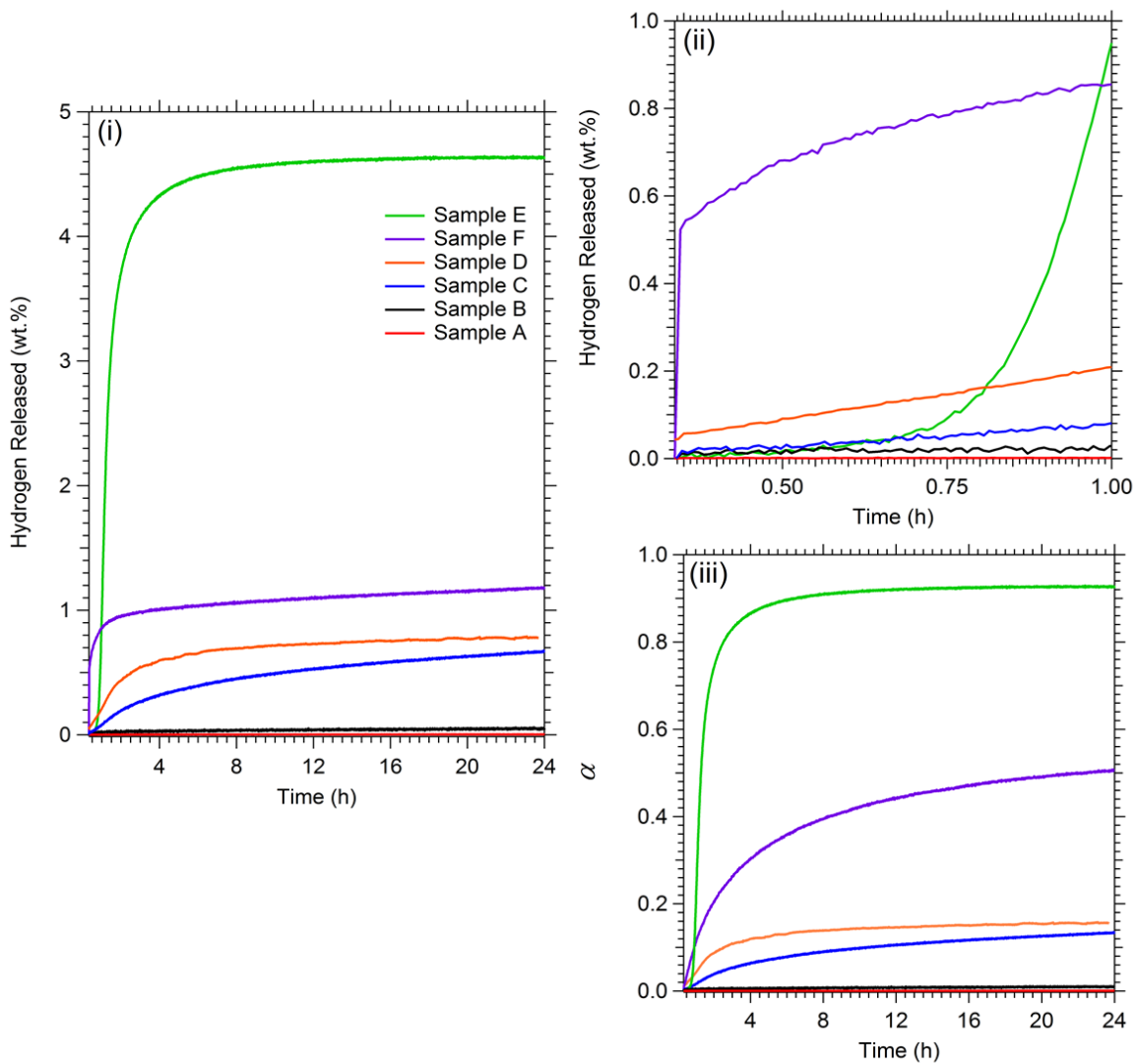
Figure 5: Rate of reaction (isothermal 300 °C with start at vacuum) for MgH₂ + Si of varying crystallite/grain sizes (i) Rate of desorption over 24 h (ii) Rate of desorption over 1 h (zoom of (i)) (iii) Normalised data, α (dividing final amount desorbed experimentally after 24 h by the maximum possible hydrogen capacity, 5 wt.%).

The equations in Table 2 were applied to the normalised data for each of the mixtures and an example of the results is given in Figure 6. For the hand mixed, ultrasonicated, 2 h ball milled, cryomilled and NP Si containing samples a straight line fit to the CV 3D diffusion growth controlled model had the highest regression values of > 0.8 [58]. The best model to describe the rate limiting step for the hand mixed, ultrasonicated, 2 h ball milled, cryomilled and NP Si containing samples is the CV 3D diffusion growth model. This model assumes that nucleation of Mg₂Si is relatively fast and occurs at surface boundaries [11] between Mg and Si atoms. The diffusional growth then continues from these boundaries to form bulk Mg₂Si particles (Figure 7). This is the same mechanism proposed for hydrogen absorption by Kelly *et. al.*[59] where the kinetic barrier of absorption was found to be the mass transport of Mg and Si between the Mg₂Si phase and the individual elemental phases.
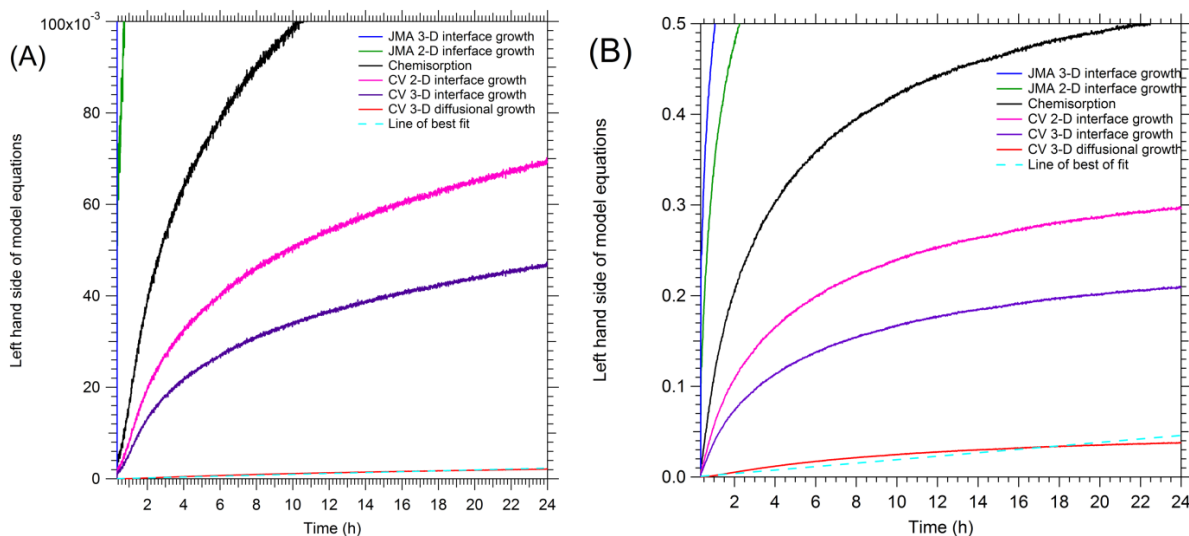
Figure 6: Results from different kinetic equations applied to the desorption data at 300°C for (A) 2 h ball milled 2MgH₂ + Si and (B) 18 h ball-milled 2MgH₂ + Si nanoparticles.
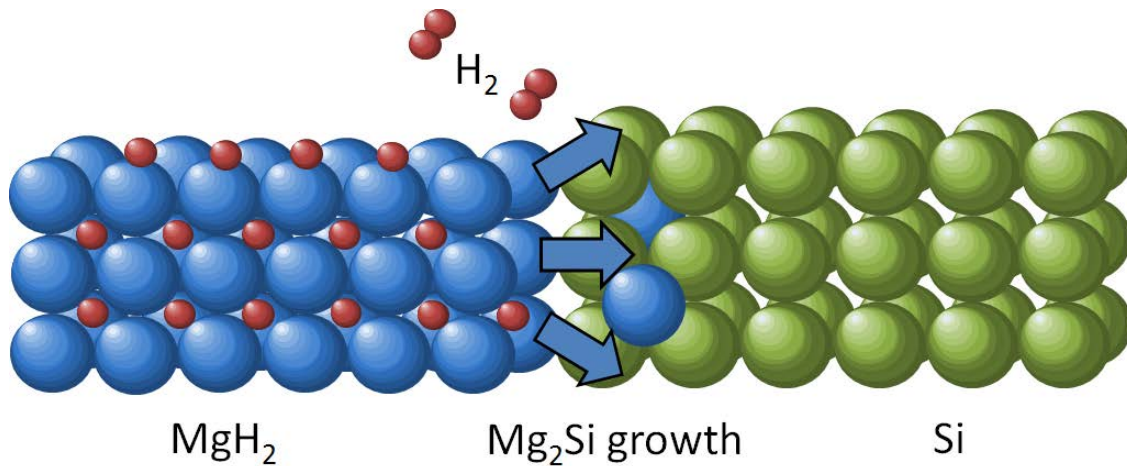
Figure 7: Schematic of the proposed reaction mechanism for the growth of Mg₂Si from the reaction between MgH₂ and Si.

The 24 h ball milled sample, however, does not fit any of the models from Table 32 with any significant confidence (Figure 8a). The discrepancy between the experimental data and mathematical models appear to be related by the aforementioned rapid change in reaction rate at 45 min, possibly due to a layer of oxidised Mg at the surface of the MgH₂ particles. If the rate of reaction is not constant with time, other variables such as the rate constant can be used as an indication of reaction behaviour [60]. However, in the case of this study, k is determined directly from the best fit model and cannot be used in this way. Instead, a wider range of mathematical models were employed to analyse the data and are given in Table 3. The results of applying these models to the experimental data are given in Figure 8b. Once again, none of the models were able to produce a linear relationship. Therefore, the reaction model for this data is more complicated than simple homogenous kinetic behaviour with the possibility of multiple smaller reactions simultaneously. As a result, the reaction constant, k, could not be calculated for the sample that had been ball milled for 24 h.

Table 3: Expanded set of reaction kinetic model equations [47].

Model Equation	Description
$\alpha^{1/2} = kt$	Power law (P2)
$\alpha^{1/3} = kt$	Power law (P3)
$\alpha^{1/4} = kt$	Power law (P4)
$[-\ln(1-\alpha)]^{1/4} = kt$	JMA interfacial growth (A4)

$\alpha^2 = kt$	1D diffusion (D1)
$[(1 - \alpha)ln(1 - \alpha)] + \alpha = kt$	2D diffusion (D2)
$[1 - (1 - \alpha)^{1/3}]^2 = kt$	Jander 3D diffusion (D3)
$1 - (2/3)\alpha - (1 - \alpha)^{2/3}$	Ginstling-Brounshtein (D4)
$\alpha = kt$	Zero order or surface controlled [49] (F0)
$-ln(1 - \alpha) = kt$	First order (F1)
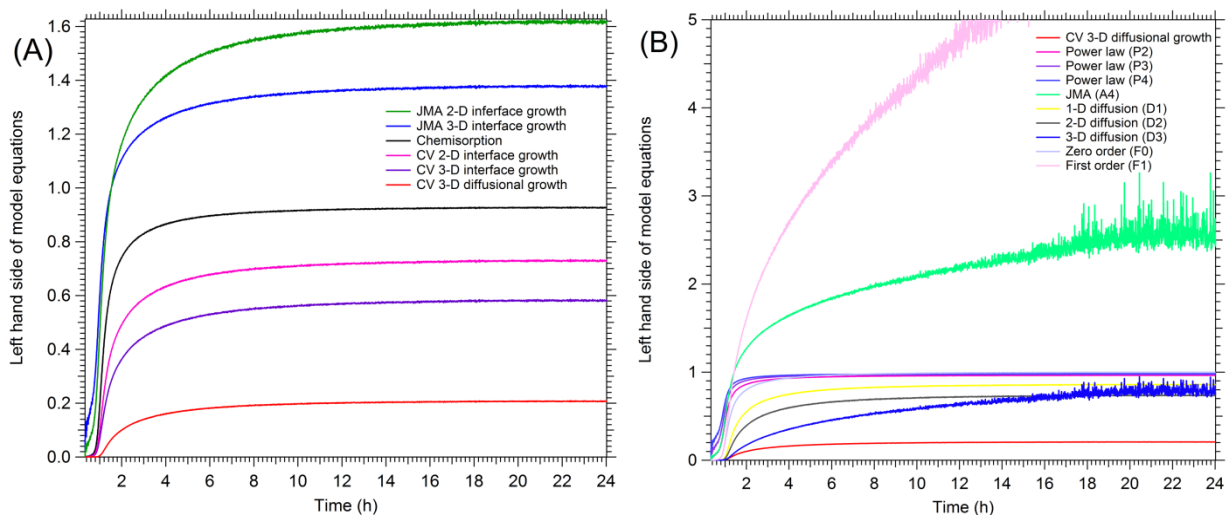
Figure 8: Results from kinetic equations applied to the desorption data at 300°C of 2MgH$_2$ + Si ball-milled for 24 h. (A) Equations from Table 2 (B) Equations from Table 3 with CV 3-D diffusion model for comparison.

The reaction rate constant values that were calculated for the other samples are given in Table 5. These were calculated using the Igor Pro (Version 6.02A, Wavemetrics, Oregon, 2007) linear fit function. The error is automatically reported at a 95% confidence interval from this function. The hand mixed sample and ultrasonicated sample have similar *k* values within error and the reaction rate increases with a decrease in crystallite size. This type of reaction kinetic improvement has been widely studied [50, 61-63].

The relationship between the activation energy, E_a and the rate constant *k* is given by the Arrhenius equation (Eqn. 4). Since E_a was determined using the Kissinger method and *k* from fitting model equations to isothermal kinetic data, the final kinetic parameter in the Arrhenius equation, the pre-exponential factor, *A*, can be calculated. *A* is determined at the same

17

temperature at which kinetic data was obtained, 300°C and the resulting values are also in Table 5 and as expected show the same relationship to crystallite/grain size as the other parameters, E_a and k.

Eqn. 4 $$k = Ae^{-\frac{E_a}{RT}}$$

Each of the reactions shown in Figure 5(A) were continued beyond 24 h for a total of 72 h at 300°C to allow the desorption reaction to go as close to completion as possible. Again, XRD was performed to identify the phases present and to calculate crystallite size for the crystalline materials (Figure 9 and Table 4). The results show that the hand mixed sample suffered kinetically due to the larger grain and crystallite size of the reactants with only 10 wt.% Mg_2Si conversion. Surprisingly, no Mg_2Si was detectable for the ultrasonicated sample. This could be due to slow kinetics thus producing nanocrystalline or small quantities present that are not XRD visible. The sample that was ball milled for 2 h contained approximately 38 wt.% Mg_2Si, which correlates well with hydrogen content obtained from the Sieverts apparatus.

Table 4: Rietveld analysis after dehydrogenation.

2MgH$_2$ + Si	Phase	Crystallite Size (nm)
(A) Hand Mixed 5 min	Mg$_2$Si	58 ± 2
R_{wp} = 6.1%	β-MgH$_2$	212 ± 4
	Mg	126 ± 11
	Si	180 ± 4
(B) Ultrasonicated 2 h	Mg$_2$Si	
R_{wp} = 6.1%	β-MgH$_2$	178 ± 3
	Mg	125 ± 17
	Si	150 ± 3
(C) Ball-milled 2 h	Mg$_2$Si	66 ± 0.7
R_{wp} = 5%	β-MgH$_2$	98 ± 1.5
	Mg	
	Si	133 ± 3
	MgO	1.8 ± 0.1
(D) Cryomilled 2 h	Mg$_2$Si	34 ± 0.8
R_{wp} = 3%	β-MgH$_2$	28 ± 0.2
	Mg	51 ± 3
	Si	58 ± 0.5
	MgO	2.4 ± 0.1
(E) Ball-milled 30:1 24 h	Mg$_2$Si	57 ± 0.4
R_{wp} = 4.5%	Mg	1 ± 0.6
	Si	63 ± 9
	MgO	2.6 ± 0.2
(F) Ball-milled MgH$_2$ 18 h	β-MgH$_2$	12 ± 0.4
+ NP Si	Mg$_2$Si	6 ± 0.2
R_{wp} = 4.7%	Si	
	MgO	3 ± 0.1

Cryomilled samples, 2 h and NP Si mixture, show high quantities of MgO present after dehydrogenation. This implies that this method of mixing exposes the sample to O$_2$ at some stage if the seal of the milling vial was compromised. This would also explain why these two sample did not achieve close to theoretical hydrogen capacity (5 wt.%) despite small grain/crystallite sizes. It can be seen from the XRD pattern for the 24 h ball milled sample that no MgH$_2$ remains. There is a small amount of MgO in the sample after hydrogen desorption together with trace amounts of Si, Mg and SS316. This accounts for the sample releasing 4.63 wt.% instead of the theoretical value of 5 wt.% H$_2$. This sample also underwent complete desorption in the fastest time of under 16 h.
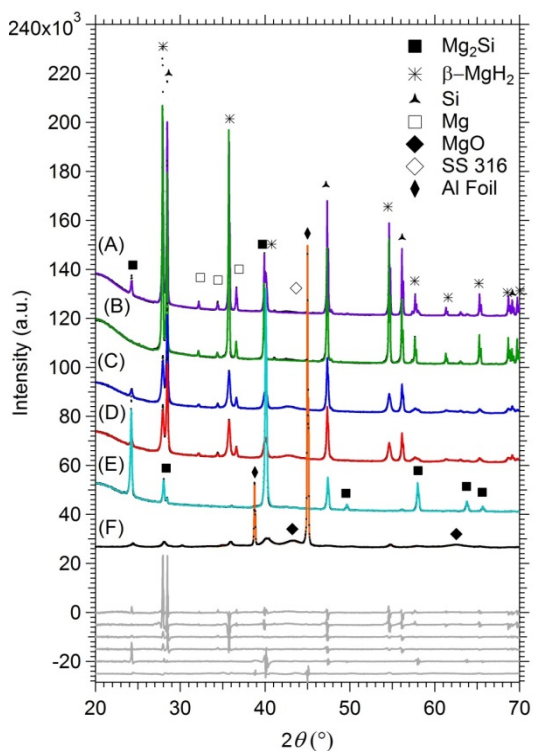
Figure 9: XRD patterns after desorption of 2MgH₂ + Si (A) mixed in a vial by hand for 5 min (B) ultrasonicated in THF for 1 h (C) ball-milled BTP 10:1 2 h (D) cryomilled for 2 h (E) ball-milled BTP 30:1 24 h (F) ball-milled MgH₂ for 18 h with synthesised Si nanoparticles, 13 nm.

Conclusion

The desorption kinetics of MgH_2 and Si have been studied for a range of crystallite/grain sizes. The kinetic parameters for this reaction have been determined and include nucleation activation energy, E_n, growth activation energy, E_a, the rate constant, k, and the pre-exponential factor, A. The Kissinger method was used to calculate the activation energies and it was found that E_a strongly correlates with crystallite size of the reactants. However, no such trend was evident for E_n. The rate limiting mechanism for the reaction was found to be most likely CV 3D diffusion. This indicates that nucleation occurs at the surfaces/interfaces at a fast rate followed by slow diffusion of H out of the Mg matrix whilst Si bonds with the Mg as it moves through the Si matrix to form Mg_2Si. Oxygen contamination played an important role in the early stages of the reaction and can account for slow kinetic behaviour as well as the low conversion rate, especially for the samples that had been cryomilled. It appears that the relationship between the reaction kinetic parameters and crystallite size is directly proportional; the smaller the crystallite size the faster the kinetics, however, more data with differing MgH_2 and Si crystallite or grain sizes is required to confirm these results. A systematic study varying ball milling

conditions and accurately measuring the grain and crystallite sizes would lead to a wider range therefore confirming the results found here.

Table 5: Summary of desorption reaction parameters and total wt.% desorbed.

Process	Crystallite size (nm)	Nucleation Activation Energy E_n (kJ mol^{-1})	Growth Activation Energy E_a (kJ mol^{-1})	Rate limiting step	Rate constant, k (h^{-1})	Pre-exponential factor, A (h^{-1})	Total H$_2$ wt.% desorbed (72 h)
Pure MgH$_2$[50]	**Ball milled**			JMA 3D growth	18×10^{-5} ($\pm 2 \times 10^{-5}$)		
Hand mixed 5 min	**β-MgH$_2$ = 207 (± 3)** Si = 173 (± 3)	-	-	CV 3D diffusion	2.90×10^{-9} ($\pm 0.02 \times 10^{-9}$)	-	$0.070\ (\pm 0.003)$
Ultrasonicated 1 h	**β-MgH$_2$ = 201 (± 3)** Si = 169 (± 3)	194.8 (± 4.9)	235.9 (± 5.9)	CV 3D diffusion	5.4×10^{-7} ($\pm 0.02 \times 10^{-7}$)	5.7×10^{-7} ($\pm 0.02 \times 10^{-7}$)	$0.160\ (\pm 0.008)$
Ball-milled 2 h	**β-MgH$_2$ = 40 (± 0.4)** Si = 134 (± 2)	355.6 (± 8.9)	187.6 (± 4.7)	CV 3D diffusion	9.7×10^{-5} ($\pm 0.02 \times 10^{-5}$)	1.0×10^{-4} ($\pm 0.2 \times 10^{-4}$)	$0.670\ (\pm 0.03)$
Cryomilled 2 h	**β-MgH$_2$ = 10 (± 0.1)** Si = 63 (± 0.6)	241.4 (± 6.0)	173.3 (± 4.3)	CV 3D diffusion	1.7×10^{-4} ($\pm 0.009 \times 10^{-4}$)	1.8×10^{-4} ($\pm 0.009 \times 10^{-4}$)	$0.89\ (\pm 0.04)$
Ball-milled 24 h	**β-MgH$_2$ = 6 (± 0.1)** Si = 46 (± 0.3)	133.5 (± 3.3)	159.8 (± 4.0)	-	-	-	$4.63\ (\pm 0.23)$
Ball- milled 18 hr MgH$_2$ NP Si	**β-MgH$_2$ = 6 (± 0.1)** Si = 13 (diameter)	253.9 (± 6.3)	234.8 (± 5.9)	CV 3D diffusion	1.9×10^{-3} ($\pm 0.006 \times 10^{-3}$)	2.0×10^{-3} ($\pm 0.006 \times 10^{-3}$)	$2.94\ (\pm 0.14)$

22

Acknowledgements

References

[1]   Sakintuna B, Lamari-Darkrim F, Hirscher M. Int. J. Hydrogen Energy 2007;32:1121

[2]   Pistidda C, Bergemann N, Wurr J, Rzeszutek A, Møller KT, Hansen BRS, Garroni S, Horstmann C, Milanese C, Girella A, Metz O, Taube K, Jensen TR, Thomas D, Liermann HP, Klassen T, Dornheim M. J. Power Sources 2014;270:554.

[3]   Vigeholm B, Vigeholm K, Jensen B, Larsen AS, Pedersen. Journal of the less-common metals 1987;131:133

[4]   Zaluska A, Zaluski L, Strom-Olsen JO. J. Alloys Compd. 1999;288:217

[5]   Borgschulte A, Gremaud R, Griessen R. Physical Review B 2008;78.

[6]   Ingason AS, Olafsson S. Thin Solid Films 2006;515:708

[7]   Mintz MH, Mintz Z, Gavra Z, Hadari. J. Inorg. Nucl. Chem. 1978;40:765

[8]   Fernández JF, Sánchez CR. J. Alloys Compd. 2002;340:189

[9]   Huot J, Liang G, Boily S, Van Neste A, Schulz R. J. Alloys Compd. 1999;293–295:495.

[10]   Imamura H, Tanaka K, Kitazawa I, Sumi T, Sakata Y, Nakayama N, Ooshima S. J. Alloys Compd. 2009;484:939

[11]   Barkhordarian G, Klassen T, Bormann R. J. Alloys Compd. 2006;407:249

[12]   Barkhordarian G, Klassen T, Bormann R. Scripta Mater. 2003;49:213.

[13]   Barkhordarian G, Klassen T, Bormann R. The Journal of Physical Chemistry B 2006;110:11020.

[14]   Ryden J, Hjörvarsson B, Ericsson T, Karlsson E, Krozer A, Kasemo B. Journal of the Less Common Metals 1989;152:295

[15]   He YP, Zhao YP, Huang LW, Wang H, Composto RJ. Appl. Phys. Lett. 2008;93.

[16]   Feliu S, Maffiotte C, Samaniego A, Galván JC, Barranco V. Electrochim. Acta 2011;56:4554.

[17]   Feliu Jr S, Samaniego A, Bermudez EA, El-Hadad AA, Llorente I, Galván JC. Materials 2014;7:2534.
[18]   Nørskov J, Houmøller A, Johansson P, Lundqvist B. Phys. Rev. Lett. 1981;46:257
[19]   Gross KJ, Spatz P, Zuttel A, Schlapbach L. J. Alloys Compd. 1996;240:206
[20]   Huot J, Liang G, Boily S, Van Neste A, Schulz R. J. Alloys Compd. 1999;293 – 295:495
[21]   Hanada N, Ichikawa T, Orimo S-I, Fujii H. J. Alloys Compd. 2004;366:269
[22]   Wronski Z, Varin RA, Chiu C, Czujko T, Calka A. J. Alloys Compd. 2007;434 – 435:743
[23]   Gerasimov KB, Konstanchuck IG, Chizhik SA, Bobet JL. Int. J. Hydrogen Energy 2009;34:1916
[24]   Dornheim M, Doppiu S, Barkhordarian G, Boesenberg U, Klassen T, Gutfleisch O, Bormann R. Scripta Mater. 2007;56:841
[25]   Ma T, Isobe S, Morita E, Wang YM, Hashimoto N, Ohnuki S, Kimura T, Ichikawa T, Kojima Y. Int. J. Hydrogen Energy 2011;36:12319
[26]   Oelerich W, Klassen T, Bormann R. J. Alloys Compd. 2001;315:237
[27]   Bonatto Minella C, Pellicer E, Rossinyol E, Karimi F, Pistidda C, Garroni S, Milanese C, Nolis P, Baró MD, Gutfleisch O. The Journal of Physical Chemistry C 2013;117:4394.
[28]   Pitt MP, Paskevicius, M., Webb, C. J., Sheppard, D. A., Buckley, C. E., Gray, E. M.,. Int. J. Hydrogen Energy 2012;37:4227
[29]   Friedrichs O, Aguey-Zinsou F, Fernandez JA, Sanchez-Lopez J, Justo A, Klassen T, Bormann R, Fernandez A. Acta Mater. 2006;54:105.
[30]   Stander C. Z. Phys. Chem. 1977;104:229.
[31]   Kelkar T, Pal S. J. Mater. Chem. 2009;19:4348
[32]   Vajo JJ, Mertens F, Ahn CC, Bowman RC, Fultz B. J. Phys. Chem. B 2004;108:13977
[33]   Bystrzycki J, Polanski M, Plocinski T. J. Nanosci. Nanotechnol. 2009;9:3441
[34]   Chaudhary A-L, Paskevicius M, Sheppard DA, Buckley CE. J. Alloys Compd. 2015;623:109.
[35]   Chaudhary A-L, Sheppard DA, Paskevicius M, Webb CJ, Gray EM, Buckley CE. J Phys Chem C 2014;118:1240.
[36]   Chaudhary A-L, Sheppard DA, Paskevicius M, Saunders M, Buckley C. RSC Advances 2014;42:21979.
[37]   Vajo JJ, Salguero TT, Gross AF, Skeith SL, Olson GL. J. Alloys Compd. 2007;446 – 447:409
[38]   Chu WK, Lau SS, Mayer JW, Müller H, Tu KN. Thin Solid Films 1975;25:393
[39]   Paskevicius M, Sheppard DA, Buckley CE. J. Am. Chem. Soc. 2010;132:5077
[40]   Manchester FDaS-M, A. Phase diagrams of binary hydrogen alloys. Materials Park, OH: ASM International, **2000**.
[41]   Suryanarayana C. Prog. Mater Sci. 2001;46:1.
[42]   Machida M, Eguchi K, Arai H. J. Am. Ceram. Soc. 1988;71:1142
[43]   Kissinger HE, Kissinger. Anal. Chem. 1957;29:1702
[44]   Boswell PG. J. Therm. Anal. 1980;18:353
[45]   Bohmhammel K, Christ B, Wolf G. Thermochim. Acta 1998;310:167
[46]   Gennari FC, Castro FJ, Urretavizcaya G. J. Alloys Compd. 2001;321:46
[47]   Khawam A, Flanagan DR. The Journal of Physical Chemistry B 2006;110:17315
[48]   Lang J, Eagles M, Conradi MS, Huot J. J. Alloys Compd. 2014;583:116.
[49]   Jacobs P, Tompkins F. Chemistry in the solid state 1955;184:212.
[50]   Dal Toè S, Lo Russo S, Maddalena A, Principi G, Saber A, Sartori S, Spataru T. Materials Science and Engineering: B 2004;108:24
[51]   Khawam A, Flanagan DR. The Journal of Physical Chemistry B 2006;110:17315.

[52]   Avrami M. The Journal of Chemical Physics 1939;7:1103.

[53]   Avrami M. The Journal of Chemical Physics 1940;8:212.

[54]   Avrami M. The Journal of Chemical Physics 1941;9:177.

[55]   Carter RE. The Journal of Chemical Physics 1961;34:2010.

[56]   Valensi G. Compt. Rend 1936;202:309.

[57]   Janot R, Cuevas F, Latroche M, Percheron-Guegan A. Intermetallics 2006;14:163

[58]   Chaudhary A-L. Nanoparticle synthesis and the addition of group IV elements for the distabilisation of magnesium hydride. Department of Imaging and Applied Physics, Faculty of Engineering and Science, vol. Ph.D. Thesis: Curtin University, 2013. p.233.

[59]   Kelly ST, Van Atta SL, Vajo JJ, Olson GL, Clemens BM. Nanotechnology 2009;20:204017.

[60]   Upadhyay SK. Chemical Kinetics and Reaction Dynamics by Santosh K. Upadhyay. Dordrecht: Dordrecht : Springer Netherlands, 2006.

[61]   Bogerd R, Adelhelm P, Meeldijk JH, de Jong KP, de Jongh PE. Nanotechnology 2009;20.

[62]   Huot J, Tremblay ML, Schulz R. J. Alloys Compd. 2003;356:603

[63]   Imamura H, Kitazawa I, Tanabe Y, Sakata Y. Int. J. Hydrogen Energy 2007;32:2408